Understanding Ion-Beam Damage to Air-Sensitive Lithium Metal With Cryogenic Electron and Ion Microscopy

Hyeongjun Koh, Eric Detsi, Eric A Stach

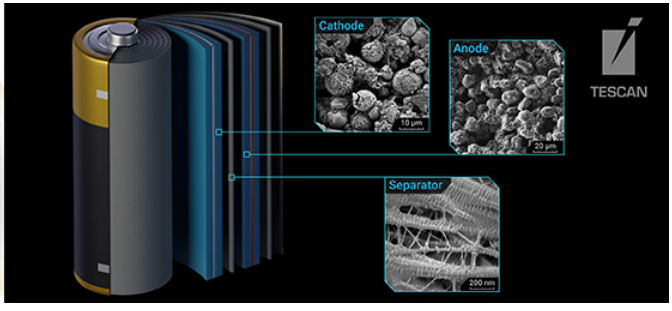

Microscopy and Microanalysis, 2023, **29**, 1350–1356
https://doi.org/10.1093/micmic/ozad074
Advance access publication 12 July 2023
Original Article

Microscopy AND Microanalysis

Understanding Ion-Beam Damage to Air-Sensitive Lithium Metal With Cryogenic Electron and Ion Microscopy

Hyeongjun Koh[1], **Eric Detsi**[1], **and Eric A. Stach**[1,2,*]

[1]*Department of Materials Science and Engineering, University of Pennsylvania, 3231 Walnut Street, Philadelphia, PA 19104, USA*
[2]*Laboratory for Research on the Structure of Matter, University of Pennsylvania, 3231 Walnut Street, Philadelphia, PA 19104, USA*

***Corresponding author:** Eric A. Stach, E-mail: stach@seas.upenn.edu

Abstract

It is essential to understand the nanoscale structure and chemistry of energy storage materials due to their profound impact on battery performance. However, it is often challenging to characterize them at high resolution, as they are often fundamentally altered by sample preparation methods. Here, we use the cryogenic lift-out technique in a plasma-focused ion beam (PFIB)/scanning electron microscope (SEM) to prepare air-sensitive lithium metal to understand ion-beam damage during sample preparation. Through the use of cryogenic transmission electron microscopy, we find that lithium was not damaged by ion-beam milling although lithium oxide shells form in the PFIB/SEM chamber, as evidenced by diffraction information from cryogenic lift-out lithium lamellae prepared at two different thicknesses (130 and 225 nm). Cryogenic energy loss spectroscopy further confirms that lithium was oxidized during the process of sample preparation. The Ellingham diagram suggests that lithium can react with trace oxygen gas in the FIB/SEM chamber at cryogenic temperatures, and we show that liquid oxygen does not contribute to the oxidation of lithium process. Our results suggest the importance of understanding how cryogenic lift-out sample preparation has an impact on the high-resolution characterization of reactive battery materials.

Key words: cryogenic-focused ion beam/scanning electron microscope (cryo-FIB/SEM), cryogenic scanning transmission electron microscopy (cryo-STEM), cryogenic transmission electron microscopy (cryo-TEM), energy storage devices, lithium metal batteries

Graphical Abstract

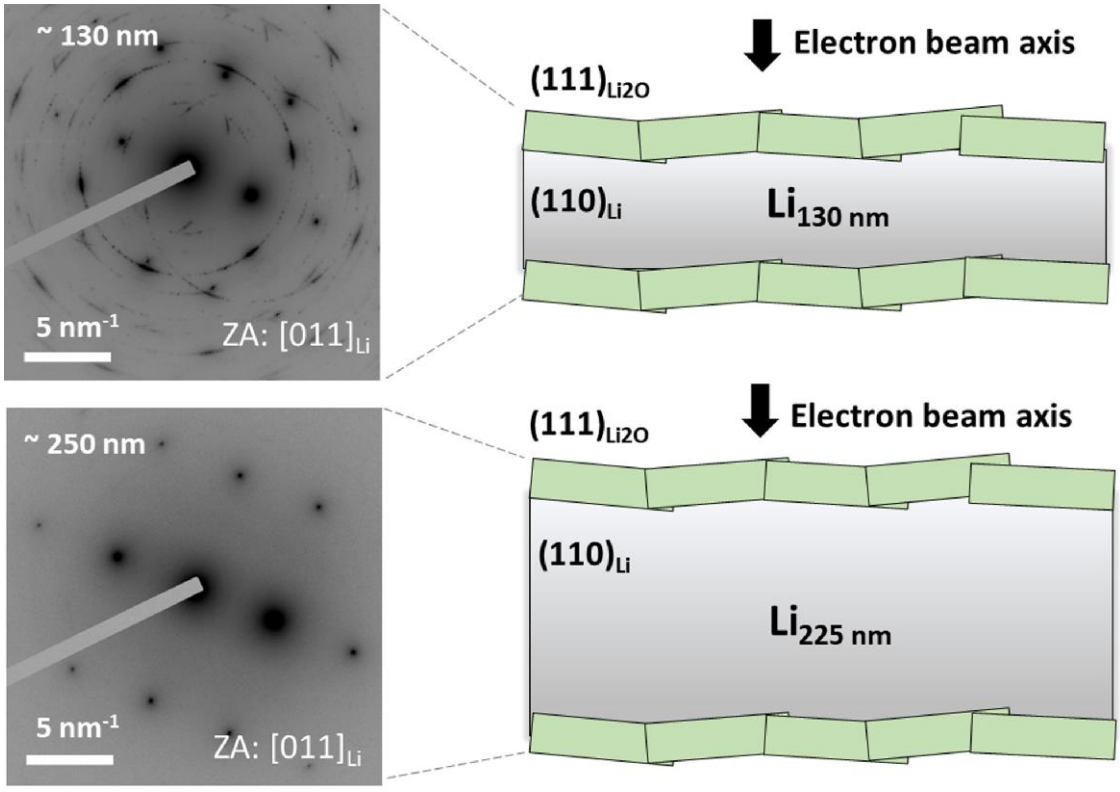

Received: May 10, 2023. **Revised:** June 18, 2023. **Accepted:** June 22, 2023

Introduction

Lithium (Li) metal has gained significant attention as an anode material for high-energy density batteries because of its low reduction potential (−3.04 V versus the standard hydrogen electrode) and the highest known gravimetric capacity (3,860 mAh/g^{1}; Lin et al., 2017). Despite dedicated efforts to enable lithium metal anodes, significant challenges persist, including the development of dead (isolated) lithium and an unstable solid-electrolyte interphase, resulting in poor cyclability (Li et al. 2018). While various characterization methods have been employed to understand these issues, high-resolution (HR) nanoscale characterization is essential (Li et al., 2017). Achieving the required magnification and resolution necessitates the use of transmission electron microscopy (TEM). Nevertheless, creating samples with the required electron transparency is challenging, given the intrinsic reactivity of lithium and its poor thermal stability (Lee et al., 2019; Zachman et al., 2020).

Because electrochemically plated Li (200–300 nm in thickness) is thin enough to be electron-transparent, many studies have relied on directly growing lithium on TEM substrates or extracting lithium particles from current collectors as a sample preparation step for cryogenic transmission microscopy (cryo-TEM; Li et al., 2017; Huang et al., 2020). However, the growth of lithium on TEM substrates may not accurately reflect the structures that would form in a standard coin cell battery configuration. Additionally, structures not directly adhered to lithium dendrites can be easily lost during the collection of Li particles from substrates (Huang et al., 2020). These observations indicate that it is necessary to prepare thin electron microscopy samples from bulk battery samples to ensure accurate HR characterization.

Cryogenic-focused ion-beam microscopy (cryo-FIB) is the best choice for controlling the thickness of beam-sensitive battery materials, as cryogenic temperatures can minimize alteration of the samples from local heat generation caused by ion-beam collisions (Zachman et al., 2018; Lee et al., 2019). In addition, the creation of TEM samples is possible at cryogenic temperatures through the cryogenic lift-out process: samples of interest can be lifted out of a specific region, attached to a TEM grid, and further thinned to the desired electron transparency (Zachman et al., 2016; Long et al., 2022). Using the cryogenic lift-out method in battery research has two potential advantages. First, the thickness of samples can be controlled regardless of the atomic number (Z) and initial sample thickness. Second, specific regions of the battery structure can be selectively extracted and preserved without losing information adjacent to the region of interest.

Despite these advantages, concerns exist regarding the possibility of ion-beam damage that might occur in battery materials, even at cryogenic temperatures, during both the cryogenic lift-out process and subsequent ion-beam milling steps required to thin the sample to electron transparency. In this work, we used a model material—lithium metal foil—to investigate whether the ion beam causes any changes in the structural and chemical properties of lithium metal. We confirm that lithium can be successfully preserved in its native state, except for the formation of a very thin oxide layer on the lithium metal. We further investigated the origin of the oxide layer by considering the Ellingham diagram, which suggests that oxidation is likely to happen when the lithium reacts with trace oxygen gas in the FIB/scanning electron microscope (SEM) chamber. These results highlight the importance of using careful sample preparation protocols during FIB sample preparation and electron microscopy to accurately characterize nanoscale features in batteries and avoid introducing experimental artifacts.

Materials and Methods

General Cryo-Lift-Out Workflow

Our TESCAN Xe plasma-FIB (PFIB)/SEM is outfitted with a Lecia cryo-FIB/SEM system, and we used workflows provided by Leica Microsystems. This includes the use of a cold stage cooled down to approximately −145°C, a sample preparation workstation, an anticontaminator, and a cryogenic vacuum transfer shuttle. Before the Li metal foils (Xiamen TOB New Energy Technology Co.) were taken out of a glove box, they were stored inside a plastic bag to minimize any potential exposure to air during the transfer. Once the foils inside the plastic bag were placed under liquid nitrogen, the bag was cut by a commercial scissor so that the quenched foils were released from the bag while fully submerged in liquid nitrogen. They were then moved to the Leica workstation (VCM) filled with liquid nitrogen and loaded with a vacuum cryogenic transfer system (VCT500). Thereafter, they were shuttled to the FIB/SEM stage. Before making a trench on the samples, ∼3 μm of organometallic platinum was deposited inside the FIB/SEM chamber on the samples to increase the quality of the cross sections. When the deposition was carried out, *in situ* and post-curing were both performed with 100 pA and 10 nA at 30 keV, respectively. We used 30 kV accelerating voltage for trenching and thinning the samples for lift-out. Initial trenching was performed at 30 nA, and a cleaning cross section was done at 10, 3, and 1 nA in series to remove curtaining effects that produce rough surfaces. Once the samples were sufficiently thinned, they were lifted out by a cold tungsten manipulator probe (Kleindeik) using redeposition welding at either 0° or 55° (Long et al., 2022). During this step, the probe was attached to the trench, and areas near the contact were milled at relatively low currents (100 and 300 pA). This process produced redeposited materials to fill the gap between the probe and the trench. Once the trenches were successfully lifted out, the lamellae were attached to copper half grids (Ted Pella), using the same redeposition welding technique. Prior to using the half grids for this lift-out step, they were welded to a Cu slot grid (Ted Pella) beforehand to manipulate the half-slot grid assembly under liquid nitrogen baths (Zachman et al., 2016). Lamellae were typically attached to the top of the half grid post, and their two ends were welded to the grid to increase mechanical resistance to bending of the lamellae. After welding to the half grid, the lamellae were thinned sufficiently to minimize multiple scattering in (S)TEM characterization. Material on the lamellae was milled from both sides, starting with 300 pA at 30 kV, with beam currents progressively decreased as the lamellae became thinner. The final thinning was done with 20 pA at 10 or 5 kV to minimize any heat-related issues potentially caused at higher voltages.

The thickness (130 and 225 nm) of lithium was carefully controlled by monitoring contrast changes in secondary electron SEM images during ion milling and via top-view SEM images.

When thinning was completed, the lamellae were transferred back to the working station filled with liquid nitrogen

via the VCT shuttle. The half-slot grid assemblies were carefully placed in cryogenic grid boxes, and the boxes were stored in a large liquid nitrogen tank before they were characterized using cryo-(S)TEM.

Cryo-(S)TEM Characterization

TEM characterization (diffraction studies and HR imaging) of these samples, including the extracted lithium metals, was performed on a JEOL F200 operating at 200 kV. The samples were transferred into the microscope with a side-entry cryogenic transfer holder (Gatan CT-3500) when the temperature was below −160°C with the cryo-shutter closed. The working station for the holder enables the transfer of the TEM grids from the cryogenic grid boxes to the groove, where TEM grids can sit on the holder under an environment of liquid nitrogen and cold nitrogen vapor to protect the reactive samples. The cryo-shutter was opened ∼20–30 min after the holder was fully inserted, and the temperature was maintained near −180°C during data acquisition. High-resolution cryo-TEM images were acquired at ∼700 $e^-/Å^2$ s for ∼0.6–1.2 s, whereas diffraction patterns were acquired at 3 $e^-/Å^2$ s for 0.6–1.2 s with a OneView camera (Gatan). We also studied the sample sensitivity to the electron beam under 200 kV. We did not see electron beam damage up to 6×10^3 $e^-/Å^2 \cdot s$ although phase contrast (i.e., Moiré patterns) in the TEM images started to drift rapidly when the dose exceeds 1×10^4 $e^-/Å^2 \cdot s$. We believe that the image drifting at such a high-dose rate results not from electron beam damage but from the sample drifting due to overheating or evaporation of the organometallic Pt mask. The HR images of the cryo-lift-out lithium at each dose rate are in Supplementary Figure S9.

The Li_2O diffraction patterns displayed in Supplementary Figure S3 were taken on a JEOL F200 operated at 200 kV with a direct electron detector (Metro, Gatan), using the same cryo-transfer holder. Cryogenic-STEM electron energy loss spectroscopy (cryo-STEM EELS) was performed on an aberration-corrected (probe-corrected) JEOL NEOARM operating at 200 kV with a cold field emission gun. A probe current of 62.5 pA measured by a K2 camera (Gatan) and a camera length of 4 cm were used. A Gatan Imaging Filter was used to collect EELS with a 5 mm aperture, and the energy dispersion was 0.25 eV for all EELS data in this paper. The pixel dwell times of the Li-K edge EELS spectra were 0.5 ms, whereas the O-K edge spectra were collected at 50 ms of pixel dwell times. The collection semi-angle for the EELS data for the Li-K edge and the O-K edge was 41.6 mrad (4 cm camera length).

Results and Discussion

Figure 1a illustrates a lift-out sample in the cryo-FIB, and Figure 1b shows a cryo-TEM image of the lithium following cryo-lift-out. There was marginal ice contamination on the TEM lamellae, as indicated by the arrows in Figure 1b. The ice contamination tends to occur during the transfer between the cryo-FIB and the cryo-TEM column. The ice that forms on the TEM lamellae consists primarily of a hexagonal, close-packed structure and tended to be sublimated during TEM imaging at a dose rate >5 $e^-/Å^2$ s (Supplementary Fig. S1). Most HR TEM images acquired in this paper were taken at a dose rate of ∼700 $e^-/Å^2$ s. Thus, the ice crystallites spontaneously disappeared during initial HR imaging. We also found that the ice did not cause any adverse effects on the Li metal during the acquisition time (Supplementary Fig. S2).

After tilting to a specific zone using the alpha tilt in the TEM goniometer, we found that the lamellae prepared by cryo-lift-out were mainly composed of a single crystal of lithium. This observation strongly suggests that the ion milling performed at cryogenic temperatures does not cause significant damage to the crystal structure of the lithium. Figures 2a and 2c display diffraction patterns of lithium cryo-lift-outs of 130 and 225 nm thickness, respectively. The selected area diffraction patterns can be indexed to the body-centered cubic (BCC) crystal structure of Li near the [110] zone axis. Simulated, indexed diffraction patterns from the two different thicknesses are presented as Figures 2b and 2d, respectively. The polycrystalline diffraction rings of the thin Li lamella (130 nm) shown in Figure 2a correspond to the face-centered cubic (FCC) structure of Li_2O (Fig. 2b). We also found double diffraction of Li_2O caused by the strongest $\pm\{110\}_{Li}$ reflections due to dynamical scattering in the sample at 130 nm thickness (Figs. 2a, 2b). The observation of strong, single crystal diffraction features, along with the polycrystalline double diffraction patterns, indicates that cryo-lift-out lithium is comprised of Li metal with a shell of oxide layers on its outer surfaces. Furthermore, the strong sixfold symmetry of Li_2O (220) diffraction rings in Figures 2a and 2b indicates a preferential orientation of the oxide with the lithium substrate. Although the formation of the oxide is textured, the orientation relationship between Li and Li_2O is approximately Li_2O {111}/Li {110} in-plane and Li_2O $[11\bar{2}]$/Li $[\bar{1}1\bar{2}]$ in-axis, a commonly observed

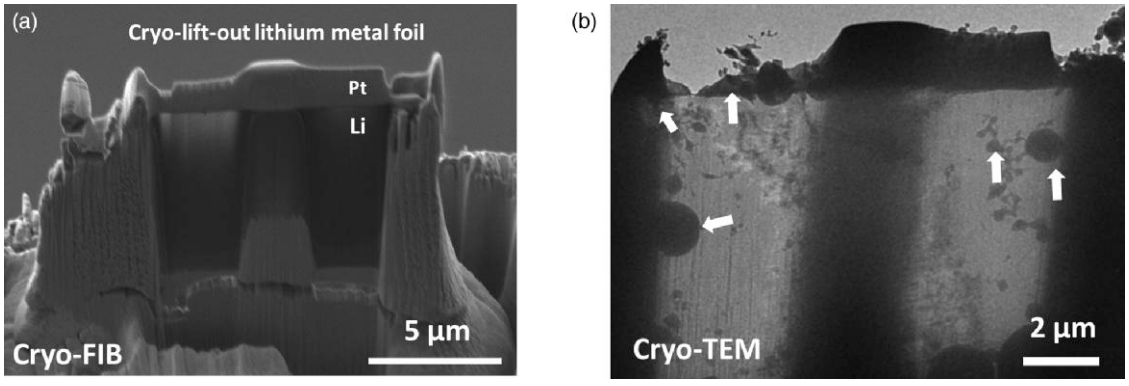

Fig. 1. Generation of a cryo-lift-out lamella from a commercial lithium metal foil: (**a**) a SEM image (2 keV) of the lithium prepared at two different thicknesses (130 and 225 nm); (**b**) a cryo-TEM image of the sample after transfer into the TEM. The arrows in white show ice contamination.

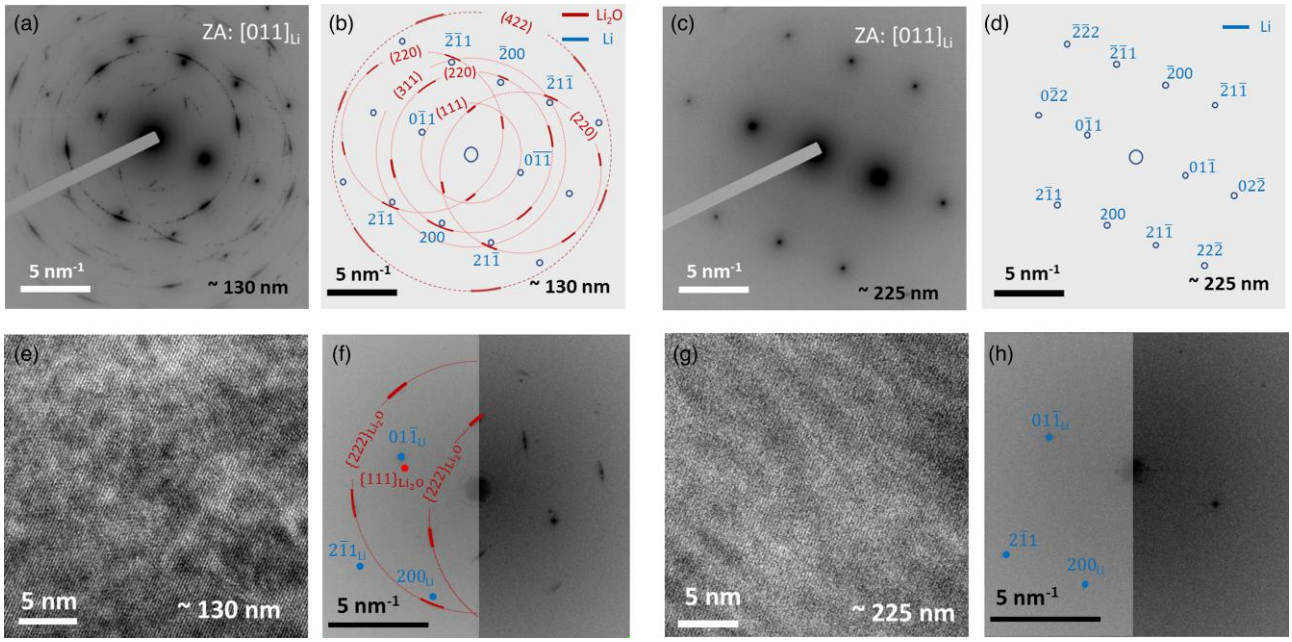

Fig. 2. Electron diffraction study of a cryogenic lift-out of lithium from commercial lithium metal foils. (**a** and **c**) Electron diffraction patterns of the lift-out sample with (**a**) 130 nm thickness and (**c**) 225 nm thickness, along the [111] zone axis of a lithium single crystal. (**b** and **d**) Simulations of the corresponding diffraction patterns show that the (**b**) 130 nm and (**d**) 225 nm thick lift-out samples are both comprised of single crystal lithium, while the patterns from polycrystalline Li_2O are present in the 130 nm thick sample. (**e** and **g**) High-resolution TEM images of (**e**) the 130 nm thick sample and (**g**) the 225 nm thick sample. (**f** and **h**) FFT patterns of the corresponding HRTEM images of the (**f**) 130 nm thick sample and the (**h**) 225 nm thick sample also show that the lift-out lamellae were a lithium single crystal, with the Li_2O formation noticable only in the 130 nm thick lamella. Note that the double diffraction from Li_2O still appeared in the FFT patterns of the lamella.

orientation relationship found in epitaxial interfaces between FCC and BCC crystals (Kang et al., 2012).

Compared with the diffraction patterns of the thin lithium sample, there is no noticeable Li_2O diffraction from the thick Li lamellae (Figs. 2c, 2d). However, diffraction patterns acquired using a more sensitive direct electron detector (Metro, Gatan) show that Li_2O clearly exists on the thick Li substrate (Supplementary Fig. S3). The suppressed Li_2O diffraction patterns from the thick sample in Figures 2c and 2d indicate that the relative thickness ratio between Li and Li_2O in the 225 nm thick sample is significantly lower than that in the 130 nm thick sample. As a result, this is consistent with our assertion that the initial Li bulk foil was almost pure lithium metal, but the outer surface oxidized to form the lithium oxide layer. We believe that the residual oxygen gas in the vacuum chamber can react with Li to form Li_2O even at cryogenic temperatures, as will be discussed in detail later in this manuscript. Figures 2e and 2g show HR TEM images of the lithium following cryo-lift-out, from the two corresponding thickness samples (130 and 225 nm). The TEM images, along with their Fast Fourier Transformation (FFT) patterns in Figures 2f and 2h, show that the lamellae of the lithium crystals are orientated near the [110] zone axis. It is noteworthy that the electron diffraction and FFT patterns from the double diffraction of the thin lithium sample in Figures 2a and 2b could also be assigned to diffraction planes of other lithium compounds, such as Li_2CO_3, as it has a similar set of d-spacings to that of the double diffraction patterns. However, the diffraction pattern in Figures 2a and 2b can be attributed to double diffraction, which is consistent with simple sample oxidation. In addition, only lithium and oxygen were observed in the region of the cryo-lift-out sample, as confirmed by the EELS spectra shown in Supplementary Figure S4.

Cryo-EELS also showed that the 130 nm thick sample contains lithium oxide, whereas the oxide content is proportionately much lower in the 225 nm thick sample. Figure 3a presents the fine structure of the Li-K edge of the two different-thickness Li samples, with the Li-K edge spectra of electrochemically plated lithium dendrites and Li_2O powders as a reference. The Li-K edge with the 130 nm thick lamella appears to be a combination of lithium metal and Li_2O. On the other hand, the Li-K edge of the 225 nm thick sample shows that it primarily consists of lithium metal, compared with that of an electrochemically deposited Li dendrite with a 200 nm thickness. However, it was still partially oxidized, which can be confirmed by the presence of an EELS O-K edge (Supplementary Fig. S4), consistent with the diffraction results above. To summarize, Li_2O mainly exists at the surface of the bulk Li core in the two lamellae regardless of thickness, and it preferentially grows with an epitaxial relationship between the Li_2O_{FCC} and the Li_{BCC} crystals. However, the relative quantities of lithium metal and Li_2O are different in the two samples, as shown in Figure 3b.

We believe that the origin of oxygen from the cryo-lift-out lithium lamellae arises from oxygen gas (O_2) in the FIB/SEM chamber. The thermodynamics of Li_2O formation with a trace amount of oxygen in the chamber can be deduced by the Ellingham diagram, as shown in Figure 3c. The diagram can be constructed by two representative lines to describe the following thermodynamic values as a function of temperature: Gibbs free energy change (ΔG) of oxygen gas at a given partial pressure (P_{O_2}: $\sim 6 \times 10^{-5}$ Pa or $\sim 6 \times 10^{-10}$ atm) in the FIB/SEM chamber and Gibbs free energy change (ΔG) of Li_2O formation (Xia et al., 2018). The diagram concludes that oxidation is thermodynamically favorable at any temperature below the coincident point (2,650°C) between the two lines.

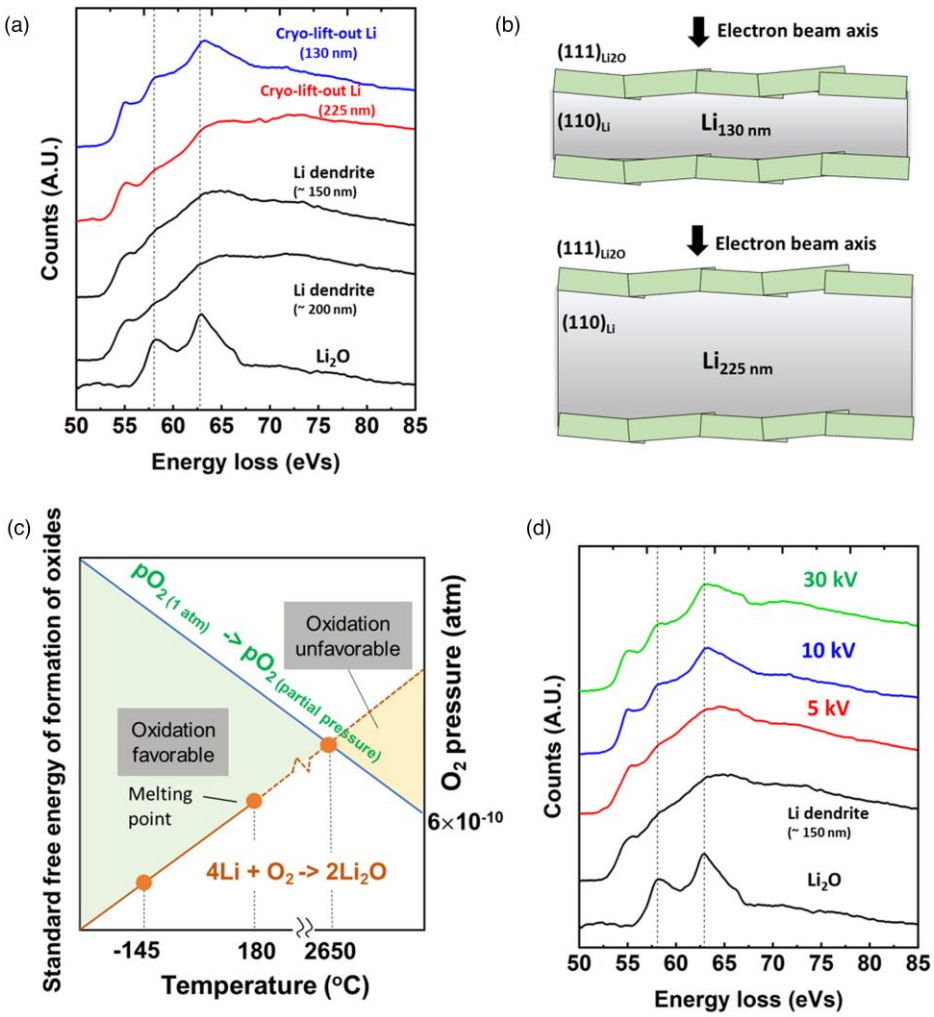

Fig. 3. Oxide formation on lithium metal in the FIB/SEM chamber at cryogenic temperatures (approximately −145°C). (**a**) Li-K edge spectra of cryo-lift-out lithium metal of two different thicknesses (130 and 225 nm) and reference materials. The reference Li-K edge spectra were collected from electrochemically plated lithium dendrites and Li_2O powders. (**b**) Schematics of the 130 and 225 nm thick cryo-lift-out lamellae consisting of Li_2O and Li along the electron beam direction. (**c**) Ellingham diagram of lithium oxide formation with two different lines describing the Gibbs free energy change of the formation of lithium oxide in orange and the Gibbs free energy change of partial pressure of oxygen in blue as a function of temperature. Above the coincident point (2,650°C), the oxidation is thermodynamically unfavorable, whereas the oxidation is favorable below that point. This indicates that the oxidation is likely to happen in the cryo-FIB/SEM chamber at cryogenic temperatures. (**d**) Li-K edge spectra from the cryo-lift-out lithium metal polished at three different voltages (30, 10, and 5 kV). The reference spectra are identical to the ones in (**a**).

Although this calculation is not valid when Li metals and Li_2O start to melt and evaporate at high temperatures, it is still valid at temperatures below the melting point of Li (180°C). Thus, this clearly indicates a strong thermodynamic driving force for lithium to react with a trace amount of oxygen in the high vacuum chamber, even at cryogenic temperatures (−145°C). Besides thermodynamics, the kinetics of the Li_2O formation is another factor to be considered, and it would be significantly suppressed at the cold temperature. However, we suspect that local heating caused by ion milling would accelerate the kinetics of oxidation at the surface of the lamellae, assisting the formation of the thin layer of the oxide layer.

While the strong driving force for the lithium oxide formation from the Ellingham diagram is a dominant factor, oxidation kinetics should also be taken into consideration, as beam-induced heating can play a role in the kinetics. The local temperature rise (ΔT) caused by the ion-beam accelerating voltage (V) can be described as follows (Ishitani & Kaga, 1995):

$$\Delta T_{\text{local}} = VI/dk\pi^{0.5} \quad (1)$$

where I is the beam current, d is the beam diameter, and k is the thermal conductivity of lithium metal. As the beam diameter is affected by the ion-beam resolution at the voltages, the Rayleigh resolution criterion concludes the following equation:

$$\Delta T_{\text{local}} = \frac{VI}{dk\pi^{0.5}} = \frac{VI}{\frac{2.44}{D} \times \frac{\sqrt{2m_{\text{ion}}eV}}{h} k\pi^{0.5}} \propto \sqrt{V} \quad (2)$$

where D is the diameter of aperture, m_{ion} is the mass of the Xe ion, and e is the ionic charge. As a result, we can control beam-induced heat impact by controlling the accelerating voltage, as the local temperature rise is proportional to the square root of the accelerating voltage. Figure 3d shows the fine structures of the Li-K edge spectra from the cryo-lift-out lithium

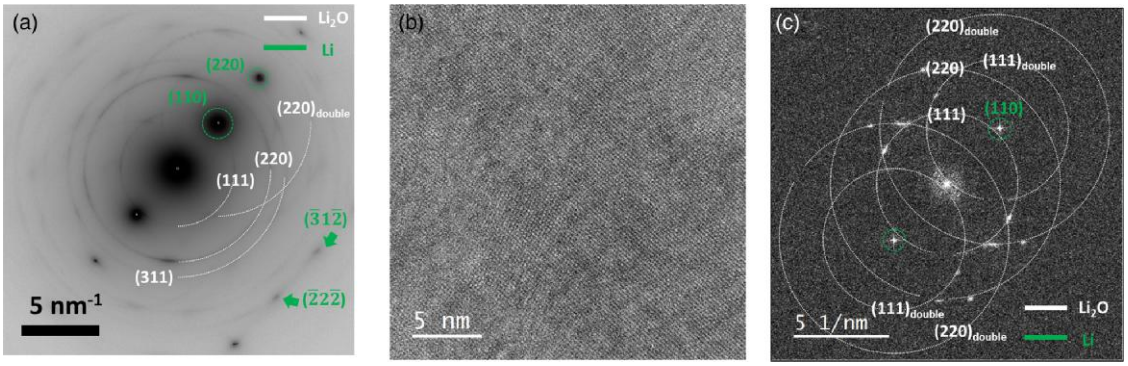

Fig. 4. Diffraction information from the cryo-lift-out lithium metal foil that did not have contact with either liquid oxygen or liquid nitrogen. This suggests that the oxidation of the lamellae mainly occurred in the cryo-FIB/SEM chamber. After the sample was prepared in the cryo-FIB/SEM, it was immediately transferred by cold nitrogen vapor to the TEM column. (**a**) Diffraction patterns, (**b**) a magnified TEM image, and (**c**) its associated FFT pattern of the cryo-lift-out lithium lamella. "Double" in the diffraction plane subscript for the Li_2O indicates that these features result from double diffraction. To increase the signal-to-noise ratio of the Li_2O diffraction, a direct electron detector (Metro, Gatan) was used to acquire the diffraction patterns and the HRTEM image.

lamellae that were polished at three different voltages (30, 10, and 5 kV) at the same current (20 pA). All lamellae were initially prepared by ion milling at 30 kV, but the final polishing was performed at the three different voltages to remove the outer oxidation shell that occurred at the different voltages. In addition, as the thickness also affects the ratio between Li and Li_2O as demonstrated above, all samples were prepared in similar thickness (120–140 nm) to isolate the impact of the accelerating voltage. While the Li-K edge from the lithium lamella polished at both 30 kV (green) and 10 kV (blue) appears to be a combination of Li metal and Li_2O, the fine structure of Li_2O in the lamella polished at 5 kV (red) is considerably suppressed in its Li-K edge spectra. Therefore, this observation indicates that the thickness of the oxide shell in the cryo-lift-out lithium is dependent on the accelerating voltages, which is consistent with our assumption that the beam-induced heating accelerates the kinetics of the oxidation, thus affecting the oxidation thickness. We briefly estimated the Li_2O shell thickness milled at each voltage using an EELS quantification method (Verbeeck & Van Aert, 2004). Their thickness is ~19, 17, and 3 nm in the cryo-lift-outs polished at 30, 10, and 5 kV, respectively (Supplementary Fig. S5).

The formation of Li_2O during the reaction between lithium and oxygen is particularly intriguing, especially given the range of oxide products, such as lithium peroxide and superoxide, found in lithium-oxygen (Li-O_2) batteries. Interestingly, Li_2O_2 (lithium peroxide) is generally more likely to form than Li_2O due to its lower formation Gibbs free energy and faster kinetics (Xia et al., 2018). This is a result of the reaction between Li ions in the electrolyte and oxygen gas in the battery system ($2Li^+ + 2e^- + O_2 \rightarrow Li_2O_2$).

However, the reaction involving *metallic* lithium and oxygen could behave quite differently. In our research, we found that Li_2O tends to form more readily. We observed a native oxide layer on lithium metal, as evident in Supplementary Figures S6 and S7. This Li_2O layer could have developed over time in our glove box before the TEM observation, or it may have formed during the processing and synthesis of the lithium foil in a dry air environment. Additionally, recent *in situ* environmental TEM studies have shown that lithium oxide forms on electrochemically deposited lithium under dry air or oxygen conditions. This observation aligns with our findings that Li_2O primarily forms on lithium (Li et al., 2023).

Although the oxidation caused by liquid oxygen is likely through a similar thermodynamic calculation, we found that the contribution is negligible. Indeed, liquid oxygen is present in liquid nitrogen once exposed to air (Zimmerli et al., 2010), and the lamellae were stored for a few days under liquid nitrogen that had been exposed to air. As a result, it is still possible to pose the question of whether lithium is oxidized by liquid oxygen during sample storage in liquid nitrogen. However, a similar oxidation trend was found in the cryo-lift-out lithium that did not have contact with either liquid nitrogen or liquid oxygen; the sample was prepared in cryo-FIB/SEM and immediately transferred into the TEM by cold nitrogen vapor to prevent the sample from reacting with any liquid oxygen. Figure 4 shows the diffraction information of the cryo-lift-out lithium lamella that can deduce the effect of liquid oxygen on the lithium oxidation. The diffraction patterns acquired near [$\bar{1}$12] in Figure 4a show that Li_2O still exists even though we excluded any oxygen contribution from liquid oxygen. A HRTEM image of the cryo-lift-out lithium lamella and its FFT pattern in Figures 4b and 4c also confirm the presence of Li_2O in the lamella. This strongly indicates that oxidation occurs in the cryo-FIB/SEM chamber and passivates the Li metal surface, preventing O_2 from further diffusing inside while the sample is stored in the liquid nitrogen cryogen.

The above results, especially in Figure 3d, support our hypothesis that the oxide shell mainly forms in the PFIB/SEM chamber. However, we cannot exclude the possibility that Li_2O forms to some extent during the transfer step from the cryo-FIB/SEM chamber to the TEM column. Even though the low voltage milling reduces the oxide thickness, we found an O-K edge signal that matches the fine structure of Li_2O in the lift-out lamella in Supplementary Figure S8. This result suggests that it is uncertain whether such thin Li_2O layers (~3 nm thick) in the lamella arise from oxidation in the PFIB chamber or during the transfer steps. Therefore, advanced instrumentation is needed to accurately estimate the oxidation induced by transfer steps. For example, if we develop a procedure that enables direct sample transfer from a cryo-FIB/SEM chamber to a cryo-TEM column without breaking vacuum, we can minimize and exclude any artifacts during transfer.

Conclusion

The development of methods for preparing electron-transparent samples of battery materials without introducing artifacts has become increasingly important for HR characterization using cryo-(S)TEM. In this study, we demonstrated that air-sensitive lithium metal can be prepared as thin lamellae using the cryo-lift-out technique, enabling HR cryo-TEM imaging, selected area diffraction, and cryo-STEM EELS to study the impacts of ion beam on the lithium lamellae. We found that the reactive lithium can be preserved in its native form while it is thinned to ~100–250 nm despite the oxide shell formation. We discussed the unavoidable artifact of the sample preparation processes because lithium has a strong tendency to oxidize. Through the thermodynamic calculation and the beam-induced heating, we found that the residual oxygen in the FIB/SEM chamber leads to the formation of a thin surface layer of Li_2O on cryo-lift-outs. Overall, our findings suggest that cryo-lift-out is a promising method for HR characterization of energy storage devices, particularly those containing reactive materials.

Availability of Data and Materials

The authors have declared that no data sets apply for this piece.

Supplementary Material

To view supplementary material for this article, please visit https://doi.org/10.1093/micmic/ozad074.

Acknowledgments

The authors gratefully acknowledge primary financial support from the National Science Foundation (NSF), Division of Materials Research (DMR), Future Manufacturing Research Grant #2134715. This work was carried out in part at the Singh Center for Nanotechnology, which is supported by the NSF National Nanotechnology Coordinated Infrastructure Program under grant NNCI-2025608. Additional support for the NSF through the University of Pennsylvania Materials Research Science and Engineering Center (MRSEC) (DMR-1720530). The authors also acknowledge technical assistance from Dr. Jamie T. Ford and Dr. Douglas M. Yates.

Financial Support

The current study has not received any funds from any organizations or institutions.

Conflict of Interest

The authors declare that they have no competing interest.

References

Huang W, Wang H, Boyle DT, Li Y & Cui Y (2020). Resolving nanoscopic and mesoscopic heterogeneity of fluorinated species in battery solid-electrolyte interphases by cryogenic electron microscopy. *ACS Energy Lett* **5**, 1128–1135. https://doi.org/10.1021/acsenergylett.0c00194

Ishitani TI & Kaga H (1995). Calculation of local temperature rise in focused-ion-beam sample preparation. *J Electron Microsc (Tokyo)* **44**, 331–336. https://doi.org/10.1093/oxfordjournals.jmicro.a051185.

Kang K, Wang J & Beyerlein IJ (2012). Atomic structure variations of mechanically stable fcc-bcc interfaces. *J Appl Phys* **111**, 053531. https://doi.org/10.1063/1.3693015

Lee JZ, Wynn TA, Schroeder MA, Alvarado J, Wang X, Xu K & Meng YS (2019). Cryogenic focused ion beam characterization of lithium metal anodes. *ACS Energy Lett* **4**, 489–493. https://doi.org/10.1021/acsenergylett.8b02381

Li Y, Huang W, Li Y, Pei, A, Boyle, DT & Cui Y (2018). Correlating structure and function of battery interphases at atomic resolution using cryoelectron microscopy. *Joule* **2**, 21672177. https://doi.org/10.1016/j.joule.2018.08.004

Li Y, Li Y, Pei A, Yan K, Sun Y, Wu C-L, Joubert L-M, Chin R, Koh AL, Yu Y, Perrino J, Butz B, Chu S & Cui Y (2017). Atomic structure of sensitive battery materials and interfaces revealed by cryo–electron microscopy. *Science* **358**, 506–510. https://doi.org/10.1126/science.aam6014

Li Y, Liu Q, Wu S, Geng L, Popovic J, Li Y, Chen Z, Wang H, Wang Y, Dai T, Yang Y, Sun H, Lu Y, Zhang L, Tang Y, Xiao R, Li H, Chen L, Maier J, Huang J & Hu Y-S (2023). Unraveling the reaction mystery of Li and Na with dry air. *J Am Chem Soc* **145**, 10576–10583. https://doi.org/10.1021/jacs.2c13589

Lin D, Liu Y & Cui Y (2017). Reviving the lithium metal anode for high-energy batteries. *Nat Nanotechnol* **12**, 194–206. https://doi.org/10.1038/nnano.2017.16

Long DM, Singh MK, Small KA & Watt J (2022). Cryo-FIB for TEM investigation of soft matter and beam sensitive energy materials. *Nanotechnology* **33**, 503001. https://doi.org/10.1088/1361-6528/ac92eb

Verbeeck J & Van Aert S (2004). Model based quantification of EELS spectra. *Ultramicroscopy* **101**, 207–224. https://doi.org/10.1016/j.ultramic.2004.06.004

Xia C, Kwok CY & Nazar LF (2018). A high-energy-density lithium-oxygen battery based on a reversible four-electron conversion to lithium oxide. *Science* **361**, 777–781. https://doi.org/10.1126/science.aas9343

Zachman MJ, Asenath-Smith E, Estroff LA & Kourkoutis LF (2016). Site-specific preparation of intact solid–liquid interfaces by label-free *in situ* localization and cryo-focused ion beam lift-out. *Microsc Microanal* **22**, 1338–1349. https://doi.org/10.1017/S1431927616011892

Zachman MJ, Tu Z, Archer LA & Kourkoutis LF (2020). Nanoscale elemental mapping of intact solid–liquid interfaces and reactive materials in energy devices enabled by cryo-FIB/SEM. *ACS Energy Lett* **5**, 1224–1232. https://doi.org/10.1021/acsenergylett.0c00202

Zachman MJ, Tu Z, Choudhury S, Archer LA & Kourkoutis LF (2018). Cryo-STEM mapping of solid–liquid interfaces and dendrites in lithium-metal batteries. *Nature* **560**, 345–349. https://doi.org/10.1038/s41586-018-0397-3

Zimmerli GA, Asipauskas M & Van Dresar NT (2010). Empirical correlations for the solubility of pressurant gases in cryogenic propellants. *Cryogenics (Guildf)* **50**, 556–560. https://doi.org/10.1016/j.cryogenics.2010.02.010

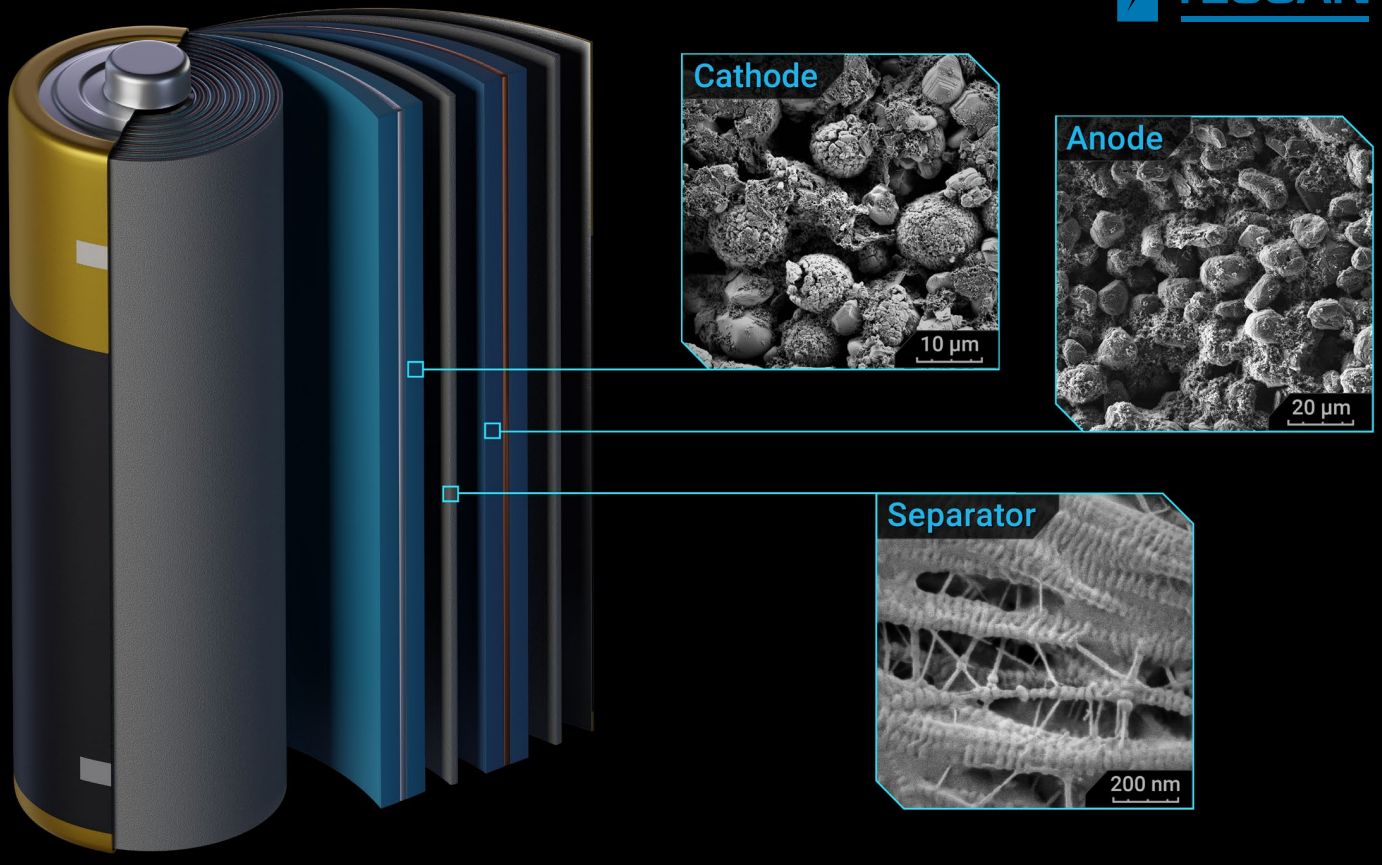

TESCAN Solutions for Battery Industry

Power your Advanced Battery Technology and Research with TESCAN Solutions

info.tescan.com/batteries

Scan for more information